I.J. Wireless and Microwave Technologies, **2026, 3, 305-322**
Published Online on June 8, 2026 by MECS Press (http://www.mecs-press.org/)
DOI: 10.5815/ijwmt.2026.03.20

Radiation-Tolerant $MASnI_3$ Perovskite Solar Cells for Space Communication: Sequential SCAPS Optimization and SRIM-Based Proton Damage Analysis

Maitry Barua
University of Chittagong, Department of Electrical and Electronic Engineering, University of Chittagong, Chittagong 4331, Bangladesh
E-mail: maitrybarua47@gmail.com
ORCID iD: https://orcid.org/ 0009-0002-9619-6580

Mohammad Mohsin
University of Chittagong, Department of Electrical and Electronic Engineering, University of Chittagong, Chittagong 4331, Bangladesh
E-mail: jitumohsin@gmail.com
ORCID iD: https://orcid.org/0009-0006-2960-0183

Sadman Al Farabe
Electronics and Telecommunication Engineering, Chittagong University of Science and Technology (CUET), Chittagong-4349, Bangladesh
E-mail: p22mete001@student.cuet.ac.bd
ORCID iD: https://orcid.org/0000-0002-4408-5881

Mizanul Hoque*
Center for Higher Studies and Research, Bangladesh University of Professionals, Mirpur, Dhaka 1216, Bangladesh
E-mail: mizan.ruetete08@gmail.com
ORCID iD: https://orcid.org/0009-0007-8398-2036
*Corresponding Author

Received: 29 January, 2026; Revised: 14 March, 2026; Accepted: 09 May, 2026; Published: 08 June, 2026

Abstract: Tin-based perovskites are among the most promising candidates for high performance light-weight and radiation-tolerant space photovoltaics, but their response to energetic proton fluxes is not adequately determined. In this work, integrated SCAPS–SRIM analysis was applied to lead-free $MASnI_3$ perovskite solar cells for space applications in order to correlate device optimization with proton-radiation response. We established a combined SCAPS–SRIM simulation platform to simulate optoelectronic behaviors and radiation tolerance of an $Au/Cu_2O/MASnI_3/TiO_2/FTO$ solar cell under AM0 illumination. Optimal-device calculations demonstrate that device absorber thickness of 0.20–0.30 μm and a TiO_2 ETL of 20–50 nm, Cu_2O HTL of 50 nm thicknesses result in good carrier collection and minimized recombination losses. Quantum efficiency and J–V measurement illustrate a stable operation under AM0 light, verifying the no extrinsic spectral incompatibility of $MASnI_3$ for the space energy source application. SRIM proton irradiation simulations (10-250 keV, 0° incidence) highlight the most damaging energy range within 50–150 keV for which masked Bragg peak lies in proximity to the $MASnI_3$ absorber and $MASnI_3/TiO_2$ interface accompanied by enhanced vacancy density, recoil energy deposition and phonon generation. High-energy protons (>200 keV) which deposit most of their damage in the rear contact stack, minimizing absorber degradation. The results overall indicate that $MASnI_3$ holds a good optoelectronic performance beyond the predictable radiation-damage behavior and thus can be considered as a promising alternative for space photovoltaic technology.

Index Terms: $MASnI_3$ perovskite; Proton irradiation; Radiation tolerance; Space solar cells; SCAPS-1D simulation; SRIM modeling; Optoelectronic properties

This work is open access and licensed under the Creative Commons CC BY 4.0 License.

1. Introduction

Long-duration missions have become almost dependent on photovoltaic (PV) power for spacecraft and planetary platforms, as the development of high-efficiency and lightweight solar cells has become an important objective for advanced space technology [1,2]. Solar arrays are the main source of power while in orbit and in deep space, and are used for attitude and orbit control, communication and telemetry, payload operation, data handling, thermal control, and, more often, electric propulsion subsystems [3]. At the extra-terrestrial AM0 spectrum (1367 Wm^{-2} at 1 AU) and in the absence of atmospheric filtering, cells are required to be efficient and stable, over several decades and towards vacuum, extreme thermal cycling, and against a hard radiation torrent, predominantly energetic electrons, protons and heavy ions from trapped belts, solar events and galactic cosmic rays [4,5]. Conventional space photovoltaics, based on Si and III-V multi-junction technologies, are primarily designed for extreme radiation hardness and flight heritage, but they tend to be bulky, inflexible, and expensive, with specific powers typically less than 3–4 W/g and a lack of suitability for large, ultra-light deployable arrays and small-sat constellations [6,7]. The series of limitations has resulted in a vigorous search for alternative absorber technologies that could provide high efficiency, high specific power, and good radiation tolerance at AM0 condition.

Perovskite solar cells (PSCs) are champion next-generation photovoltaics with >25% efficiencies, tunable bandgaps, strong absorption, solution processing, and compatibility with lightweight, flexible substrates [8]. While PSCs operate well under conditions relevant to space, they are susceptible to AM0-driven UV exposure, vacuum-driven thermal cycling, and radiation-driven ion migration [9]. In contrast, Si, GaAs, and III–V technologies have well-developed and validated JPL/NRL radiation models [10] to re-capture the, but an exhaustive PSC irradiation database is limited, especially for Pb-based absorbers such as $MAPbI_3$ and $FAPbI_3$ [11]. While these Pb-perovskites maintain 60–90% efficiency after proton fluences that degrade III–V cells, their toxicity spurs a search for Pb-free perovskites based on Sn. While $MASnI_3$ has a narrow bandgap, high absorption, and adequate mobility Sn oxidation, self-doping, and interfacial recombination require well-engineered transport layers [12,13]. All-inorganic Cu_2O HTLs and TiO_2 ETLs exhibit enhanced stability and selective carrier extraction for space environments [14,15].

With the exception of a recent numerical–experimental studies that optimized lead-free perovskite architectures, where the FTO/TiO_2/$MASnI_3$/ Cu_2O/Au configuration was identified to be a promising terrestrial option [16], these works are still restricted to AM0. It does not evaluate performance at the AM0 spectrum or exposure to space-radiation amplitudes, only AM 1.5 illumination. This trend continues through high-efficiency modelling of lead-free double perovskites [17] such as Cs_2AgBiI_6/$Cs_2AgBiBr_6$ bilayer devices that obtain PCEs >34% via band-alignment and defect-density optimization which only consider terrestrial optoelectronic behavior and neglect proton-induced displacement damage [18]. Recently published reports on vacancy-ordered Cs_2CrI_6 that exhibit outstanding proton-irradiation tolerance of 90% retention of PCE at flunce as high as 5×10^{13} protons cm^{-2} only offer a suggestive review of all Sn-based perovskites without extending their findings to Sn [9]. By comparison, proton-irradiation studies of Pb-based systems studies such as $CsPbI_3$, and mixed-cation halide perovskites show that these devices often maintain 60–90% of initial performance at fluences ranging from 10^{13}–10^{14} protons cm^{-2} [19,20], however, both similar studies are not available for $MASnI_3$. Consequently, electronic and nuclear stopping, displacement damage, recoil cascades, defect creation, as well as their effects on carrier lifetimes, mobilities and interfacial energetics in lead-free $MASnI_3$ is still unexplored. It indicates the essential conditions for the development of a SRIM-SCAPS modelling framework, complementing the modelling of SRIM proton-induced defect distributions in a manner the maps onto device-level performance, and thus allow for a sound evaluation of $MASnI_3$ based photovoltaic devices for space application.

In this work, a $MASnI_3$-based solar-cell architecture employing TiO_2 and Cu_2O as the electron and hole transport layers, respectively, is investigated based on favorable energy-band alignment. The device is systematically optimized using SCAPS-1D by varying the ETL, absorber, and HTL thicknesses together with the absorber doping concentration to identify an improved photovoltaic parameter set. The optimized multilayer structure is subsequently analyzed using SRIM to evaluate proton penetration, energy deposition, and defect-generation tendencies across the device stack under space-relevant conditions. As such, the contribution of this work is in a simultaneous investigation into device optimization and proton-radiation evaluation of $MASnI_3$ solar cells, giving specific consideration to its suitability for space photovoltaic applications.

2. Device Structure and Simulation Parameters

2.1. Solar Cell Device Modeling

With a realistic and accurate simulation of the back-end physics process in SCAPS-1D, we can analyze a large number of device designs and designs for a flexible photovoltaic device. That is why our device was modeled and optimized using SCAPS-1D. Predictions made by SCAPS-1D match well with actual experiments and results. Equation (1) portrays the Poisson's equation, that authorizes a correlation between density of charges and electric potential and allows us to understand how charge density is interrelated with electrostatics or electric potential. To calculate performance properties for a solar cell, we use the continuity equation for the charge carriers. SRH recombination statistics are used by this tool to analyze device properties for a solar cell.

$$\frac{d}{dx}\left(-\varepsilon(x)\frac{d\psi}{dx}\right)=qN_d^+(x)-qN_a^-(x)+qp(x)-qn(x) \tag{1}$$

Here, p, n, Ψ, ε, N_a^-, N_d^+ represent the ionized the total hole concentration, the total concentration of electrons, electrostatic potential, permittivity, acceptor-like doping level and the donor-like doping level. The carrier regularities are expressed as follows from equation (2) and (3):

$$\frac{\partial j_n}{\partial x}=q\frac{\partial n}{\partial t}+qR_n-qG \tag{2}$$

$$\frac{\partial j_p}{\partial x}=-q\frac{\partial n}{\partial t}-qR_p+qG \tag{3}$$

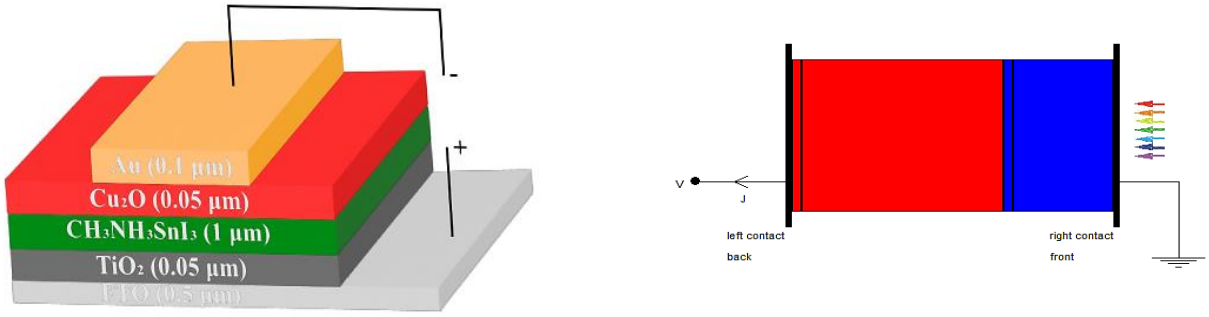
The variables j_p and j_n indicate the current densities of the carriers, holes and electrons respectively. R_p defines the number of recombining electron and hole currents per volume concentration, while G shows the rate of generation of holes per volume concentration. Considering the particular equations and boundary conditions, we used the improved SCAPS 1D program which is based on the Eg-sqrt model. The mathematical representation of the Eg-sqrt model is shown in equation (4),

$$\alpha(h\vartheta)=\left(\alpha_0+\beta_0\frac{E_g}{h\nu}\right)\left(\frac{h\nu}{E_g}-1\right)^{1/2} \tag{4}$$

Here, α, hϑ, and Eg represents the photon absorption, photon energy, and bandgap, respectively. The constants of the model, α_0 and β_0, have the same units of measure as the absorption coefficient, like cm^{-1}. These constants have a mathematical relationship with the a and b parameters of the traditional "Tauc"-based model which are defined in Equations (5) and (6):

$$\alpha_0=a(E_g)^{1/2} \tag{5}$$

$$\beta_0=\frac{b}{(E_g)^{1/2}} \tag{6}$$



(a) Proposed device structure

(b) Proposed simulated structure in SCAPS 1D

Fig. 1. Schematic Diagram of Au/Cu2O/MASnI3/TiO2/FTO configuration

In our study on lead-free MA-based PSCs, we use Cu_2O as HTL and TiO_2 as ETL, FTO as transparent conductive oxide layer and gold (Au) as support contact for metallic elements, as shown in fig. 1. FTO has a 4.4 eV occupancy function, while Au has a 5.1 electron volt function. It changes some parameters like thickness, band gap, relative permittivity, electron affinity, donor and acceptor concentration, and electron and hole mobility to quantify the performance of the cell. Device simulation involves neutral defects with a Gaussian energy distribution (standard deviation = 0.1 eV) in each layer up to 0.6 eV energy level. Both the electron and hole thermal velocities were fixed at 10^7 cm/s. Assuming the error is impersonal, the simulation is performed at 300 k subordinated to an AM 1.5G laser. The device's HTL/Perovskite and Perovskite/ETL interfacial layers show distinct electron and hole capture cross sections and defects. The defect density at the absorber/HTL and the absorber/ETL interfaces was set to 1×10^{13} cm^{-3}, with hole and electron capture cross-sections of 10^{-18} and 10^{-19} cm^2, respectively. Bulk and interfacial defects was considered for realistic device modeling. During the parametric optimization, series resistance (Rs) and shunt resistance (Rsh) were always set to constant value of 3 Ωcm² and 4200 Ωcm² respectively. Table 1. give the basic data parameters we need for

the model procedure at every degree. Where direct material-specific data were scarce, values were selected from closely aligned reports and within physically accepted ranges that appear commonly in SCAPS simulations.

Table 1. Simulation input parameters for HTL, absorber, ETL, and TCO

Parameters	Cu_2O	$CH_3NH_3SnI_3$	TiO2	FTO
Thickness, d (nm)	50	1000	50	500
Bandgap, E_g (eV)	2.17	1.61	3.2	3.5
Electron affinity, χ (eV)	3.2	4	4	4.4
Dielectric Permittivity (relative), ε_r	7.11	10	9	9
CB effective density of states, N_C (cm^{-3})	2.2×10^{18}	1×10^{18}	2×10^{18}	2.2×10^{18}
VB effective density of states, N_V (cm^{-3})	1.1×10^{19}	1×10^{19}	1.8×10^{19}	1.8×10^{19}
Electron mobility, μ_n (cm^2/ Vs)	210	1.6	20	20
Hole mobility, μ_h (cm^2/ Vs)	80	1.6	10	10
Shallow uniform acceptor density, N_A (cm^{-3})	1×10^{18}	1×10^{16}	0	1×10^{19}
Shallow uniform donor density, N_D (cm^{-3})	0	1×10^{19}	1×10^{18}	0
Defect density, N_t (cm^{-3})	1×10^{15}	1×10^{14}	1×10^{15}	1×10^{15}
References	[16]	[16,21]	[16,22]	[23]

2.2. Proton Irradiation Modelling

The SRIM/TRIM (Stopping and Range of Ions in Matter/Transport of Ions in Matter) Monte Carlo package, which is based on the Binary Collision Approximation, was used to model how the multilayer Au/Cu_2O/$MASnI_3$/TiO_2/FTO solar cell would behave when hit by protons [24,25]. In this framework, every proton-atom interaction is treated as a separate two-body collision. This makes it possible to calculate electronic and nuclear stopping, recoil cascades, vacancy generation, phonon emission, and total deposited energy at different depths. The Ion Distribution and Quick Damage Calculation modes were used to measure the effects of radiation at energies between 10 and 250 keV H^+, which are typical of low to mid-energy trapped proton spectra in space. We launched 500 protons from the Au side for each energy to make the module geometry look like it would in space. The densities of the layers (Au: 19.31 g cm^{-3}; Cu_2O: 6.00 g cm^{-3}; $MASnI_3$: 4.50 g cm^{-3}; TiO_2: 4.23 g cm^{-3}; FTO: 7.00 g cm^{-3}) and the thicknesses (0.10/0.05/1.00/0.05/5 µm) were in line with what was found in the literature. To ensure conservative estimates of displacement damage, channeling effects and subsequent lattice recovery processes were not included, following established SRIM guidelines.

3. Result and Analysis

3.1. Energy Band Analysis

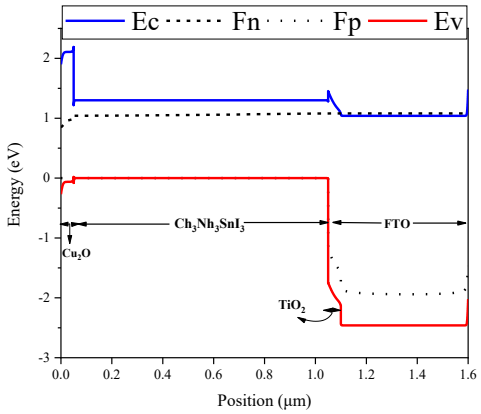


Fig. 2. Energy-band alignment of the Au/Cu_2O/$MASnI_3$/TiO_2/FTO solar structure.

The band-alignment diagram shown in fig. 2. conforms that the Au/Cu_2O/$MASnI_3$/TiO_2/FTO stack can be treated as a well-defined p–i–n junction, which contributes to the efficient charge extraction with little contribution from interfacial recombination. Cu_2O has a well-aligned valence-band offset with $MASnI_3$ allowing for selective hole transfer, and its conduction band is 0.8 eV above that of the absorber, providing an effective electron-blocking barrier, which is consistent with previous $MASnI_3$ HTL studies [26]. The flat E_c and E_v in $MASnI_3$ identifies it as an intrinsic absorber with much of the internal electric field situated at the Cu_2O/$MASnI_3$ and $MASnI_3$/TiO_2 interfaces. The strong separation of the quasi-Fermi levels (Fn–Fp) indicates efficient photogeneration, which underlies the high simulated VOC. While TiO_2 offers a well-matched electron-extraction path and hole-blocking barrier, Cu_2O blocks interfacial recombination. In general aspects, the type-II alignment and the large built-in field enable balanced carrier selectivity and robustness against space-rich photon environments [27,28].

3.2. HTL Thickness Optimization

The optimization of HTL thickness is critical as the hole-transport interface governs recombination, charge extraction, and device stability, all of which contribute directly to modelling fidelity for $MASnI_3$-based cells operating under AM0 conditions [29,30]. The HTL thickness that does not cause any parasitic absorption, which is an important criterion for an accurate SCAPS modelling of radiation-induced interfacial behavior [31–33]. As seen in the fig. 3., PCE, J_{SC}, V_{OC} and FF increase steeply below a Cu_2O thickness of 10–30 nm, indicative of increasingly effective surface passivation and lower interfacial recombination as a continuous HTL is established. Above this thin regime, all performance parameters are saturated and adding more HTL simply adds to the optical loss without electronic improvement [34]. These trends support that ultrathin 15–30 nm Cu_2O HTLs are favorable for suppressing recombination and facilitating hole extraction in $MASnI_3$ devices. The HTL thickness was set to 50 nm for the following device simulations and SRIM analysis, wherein the solar cell provided a PCE of 25.68%, V_{OC} of 1.078 V, J_{SC} of 32.0392 mA/cm^2 and FF about 74.3573%.

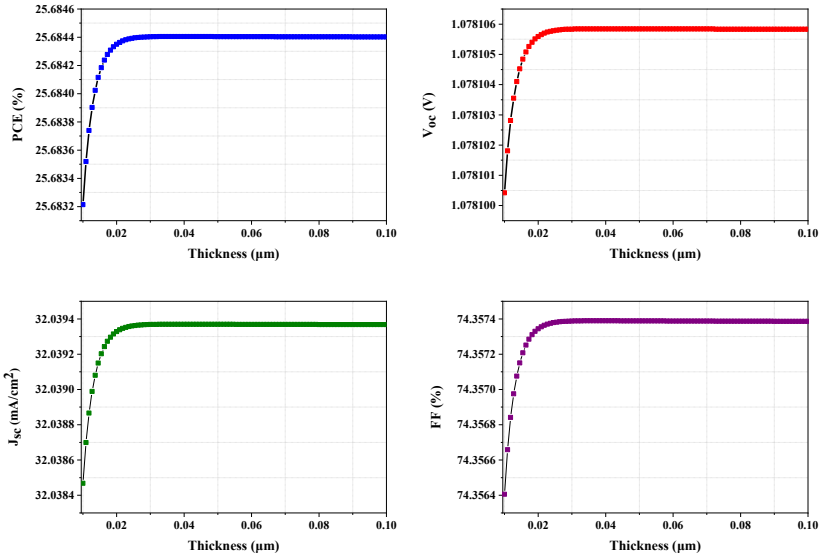


Fig. 3. Variation of PCE, VOC, JSC, and FF with Cu2O HTL thickness.

3.3. ETL Thickness Optimization

The ETL thickness is an important parameter as it determines electron extraction, interfacial recombination and optical losses, and thus its optimization is crucial to a full SCAPS–SRIM modelling of the charge transport under space-relevant AM0 spectra [35,36]. The results in fig. 4. determine a distinct ETL design window to achieve excellent carrier selectivity while securing device stability and radiation hardness [37,38]. The PCE decreases from 30.5% at 10 nm to 28.25% at 100 nm as TiO_2 thickness increases, attributed to heightened parasitic absorption and transport resistance. Similarly, the J_{SC} decreases since thicker TiO_2 layers absorb incoming photons, facilitating recombination prior to electron transit to the $MASnI_3$ interface, leading to a reduction of 1 mA/cm² from 10 nm to 100 nm. V_{OC} slightly recovers at extremely thin thicknesses due to a decreasing hole leakage, but decreases again when the intrinsic recombination starts dominating. FF decreases initially due to increased series resistance with thicker TiO_2, and then it gets stabilized after 50 nm as blocking selectivity enhances. Combined, these trends establish 20–50 nm TiO_2 as the ideal ETL thickness in terms of transparency, charge selectivity and reduced recombination losses. As such, for the subsequent device and SRIM analyses, an ETL thickness of 50 nm was chosen, as it falls within this well-defined optimum range and shows 28.7% PCE, 1.25V V_{OC}, J_{SC} of 29.6 mA/cm^2 and 77% FF.

3.4. Absorber Layer Thickness Optimization

The thickness of the $MASnI_3$ absorber also has a strong effect on the overall photon absorption, carrier transport, and recombination in the device; therefore, optimization of the thickness is important for accurate AM0 performance modelling and characterization of the radiation-induced degradation in SCAPS–SRIM simulations [22]. As shown in fig. 5., the PCE initially shows high value of above 27% with 200nm thickness less due to improved light absorption and increased photocarrier generation in the thin-film regime. J_{SC} behaves similarly, but starts to drop off after ~200–300 nm, because too thick layers put bulk recombination that limits carrier extraction into play. On the other hand, V_{OC} monotonically decreases with thickness due to greater trap-assisted recombination in thicker $MASnI_3$ films, which decreases quasi-Fermi level splitting. Moreover, as the transport length increases and the series recombination loss intensifies due to increased thickness, we find that FF also decreases, which is in line with the behavior of mobility-

limited Sn-based perovskites. Where these trends meet is for an optimal absorber thickness of 0.20–0.30 µm, where sufficient photon absorption is balanced with adequate recombination control, consistent with previous Sn-perovskite optimizations. For extraterrestrial application considerations where operation stability is a crucial issue, an absorber thickness of 1000 nm was chosen for the following analysis since the performance of devices nearly plateaus in this high-thickness region.

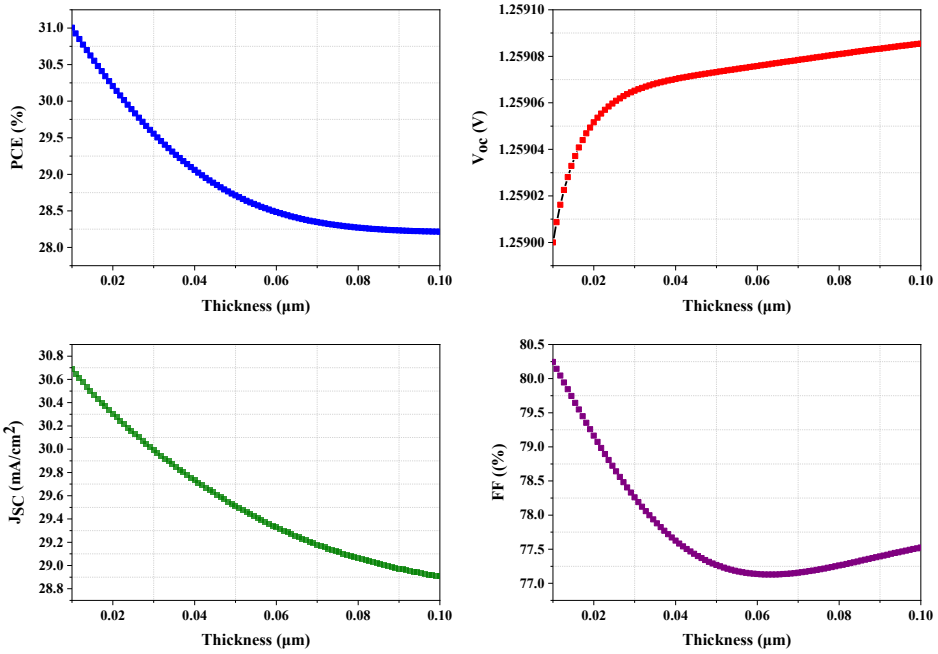


Fig.4. Variation of PCE, VOC, JSC, and FF with TiO2 ETL thickness.

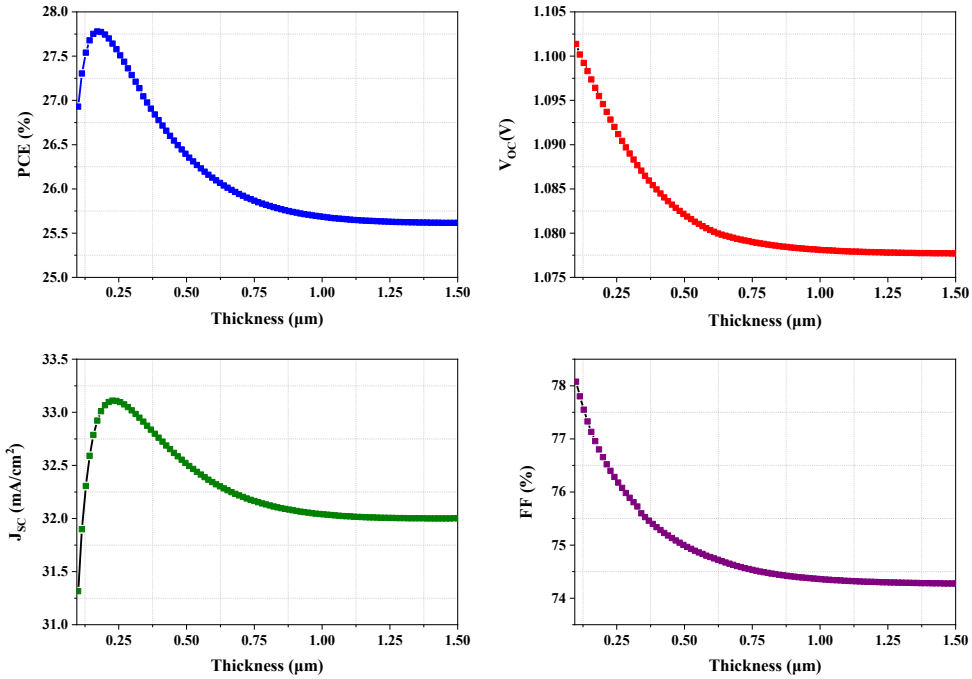


Fig. 5. Effect of $MASnI_3$ absorber thickness on photovoltaic output, including PCE, V_{OC}, J_{SC}, and FF.

3.5. Acceptor and Donor Density Variations for Absorber Layer

The acceptor and donor impurity levels determine the internal electric field, carrier lifetimes, and recombination pathways in $MASnI_3$ which, in turn, govern stability and efficiency, making defect-density engineering a prerequisite [39]. The results indicate that after weak p-type doping (10^{11} cm^{-3}) PCE sharply increases with acceptor density (up to

10^{12} cm^{-3}) as the built-in potential and carrier extraction both improve. PCE drops accordingly with increasing acceptor doping (>10^{17} cm^{-3}) due to increased SRH and Auger recombination for heavily doped Sn-perovskites. The VOC and JSC are also improved until the optimum point of doping, beyond which excessive recombination dominates. By the same token, elevated donor densities (> 10^{18} cm^{-3}) excite deep-level defect formation and curtail JSC, as well. Therefore, small intervals of p-type (10^{14}–10^{16} cm^{-3}) and n-type (<10^{15} cm^{-3}) doping lead to optimal performance, and indicate that excellent defect control is required for both high efficiency and radiation-hard performance.

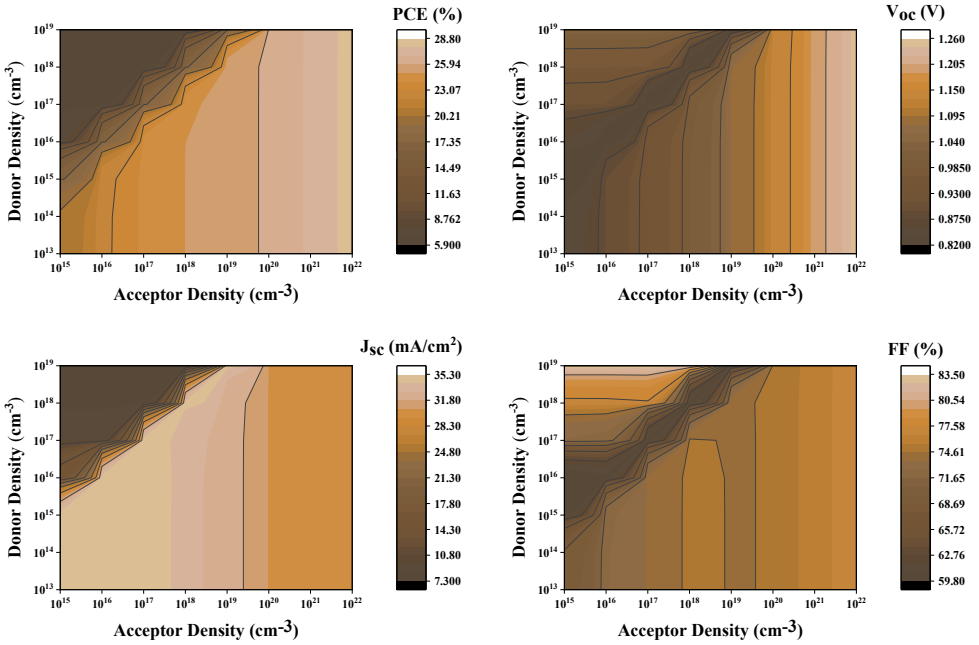


Fig. 6. Contour maps showing the influence of absorber-layer acceptor and donor densities on the photovoltaic metrics of the $MASnI_3$ device, including PCE, VOC, JSC, and FF.

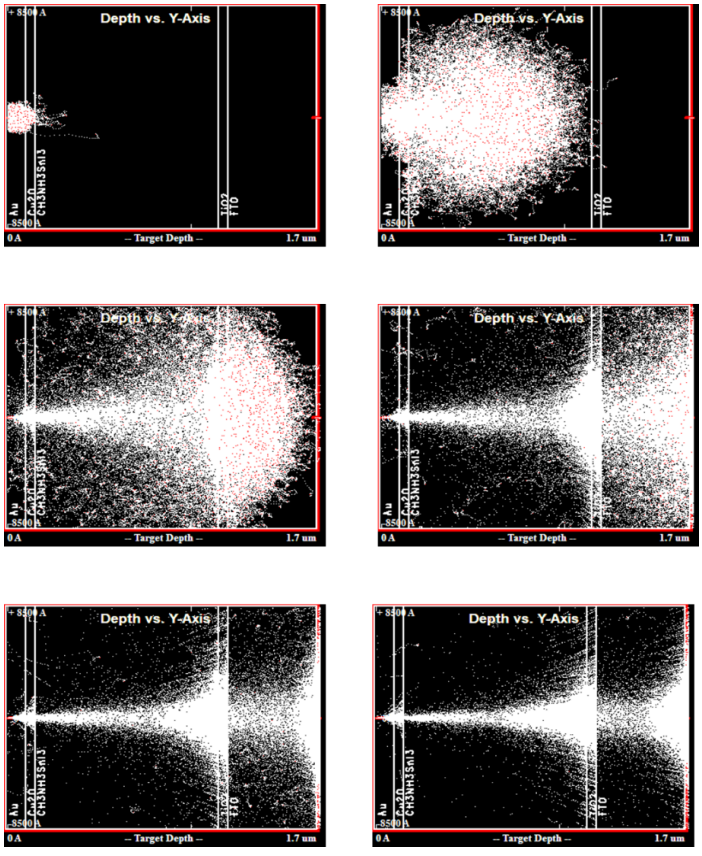


Fig. 7. Simulated proton trajectories at 10–250 keV through the $Au/Cu_2O/MASnI_3/TiO_2/FTO$ device.

4. SRIM Section Analysis

4.1. Proton Trajectories and Penetration Depth (Depth vs Y-axis)

Proton-penetration study is adequate due to high-energy proton being a dominant radiation species in the Van Allen belts and deep-space environments, the interaction of which with multilayer photovoltaic stacks is a significant factor in determining device durability for AM0 operation [40,41]. SRIM depth profiles measure the way in which energy deposition and displacement damage is allocated within the $Au/Cu_2O/MASnI_3/TiO_2/FTO$ structure permitting SCAPS–SRIM degradation modelling when creating accurate physical deep level representation, shown in fig. 7. Protons at 10 keV lose a large fraction of their energy in Au and Cu_2O, only entering the $MASnI_3$. Proton trajectories place the Bragg peak in the $MASnI_3$ bulk between 50–100 keV, resulting in maximum defect density inside the photogeneration region—consistent with NIEL trends in perovskites. As higher energy irradiations, such as 150 keV, damage get directed towards the $MASnI_3/TiO_2$ interface, identifying recombination-critical junctions become more prone to damage. Incoming protons penetrated through $MASnI_3$ and TiO_2 at 200–250 keV, with high absorption in FTO. In the end, at the active layer region of $MASnI_3$, the Bragg peak is overlapping with the region of 50–150 keV and therefore the $MASnI_3$ is the most sensitive to degradation here.

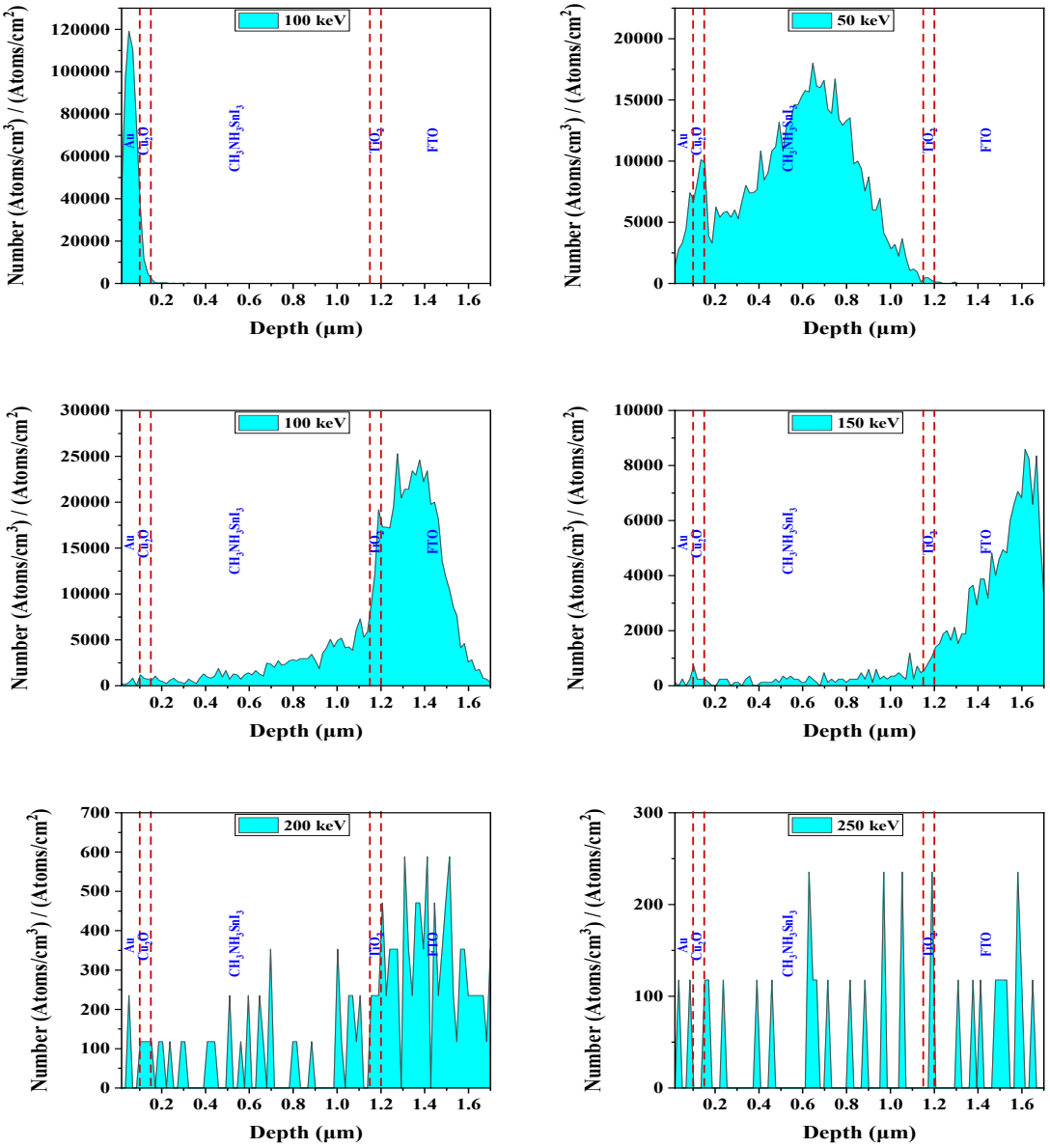


Fig. 8. Vacancy production per unit depth for 10–250 keV protons across the device stack.

4.2. Depth-Resolved Displacement Damage: Vacancy Production Rate

Vacancy-Profile analysis is important due to the role of displacement defects by energetic protons as the major cause of non-ionizing degradation in space photovoltaics, and their depth distribution defines material vulnerability to AM0 [42,43]. The SRIM vacancy curves in fig.8 show how many defects are absorbed in which layer in the $Au/Cu_2O/MASnI_3/TiO_2/FTO$ stack, so that recombination and mobility degradation modelling can be accurately integrated with SCAPS–SRIM. Vacancies are limited to Au and Cu_3O at 10 keV, suggesting purely surface damage. At 50 keV, vacancy creation enters the $MASnI_3$ bulk, indicating the beginning of absorber degradation similar to the shallow cascade vulnerability known in Sn-based perovskites. Vacancy peak positions suggest, at 100 keV, strong non-ionizing damage where recombination centers limiting diffusion length dominate at the absorber center. However, at 150 keV, peak damage shifts into the TiO_2 layer, where the $MASnI_3/TiO_2$ extraction interface is highly sensitive. Vacancies in TiO_2 and FTO dominate at 200–250keV. In aggregate, $MASnI_3$ receives its greatest displacement damage in the 50–150 keV, which is one of the key region of interest for radiation-hardening strategies for space PVs.

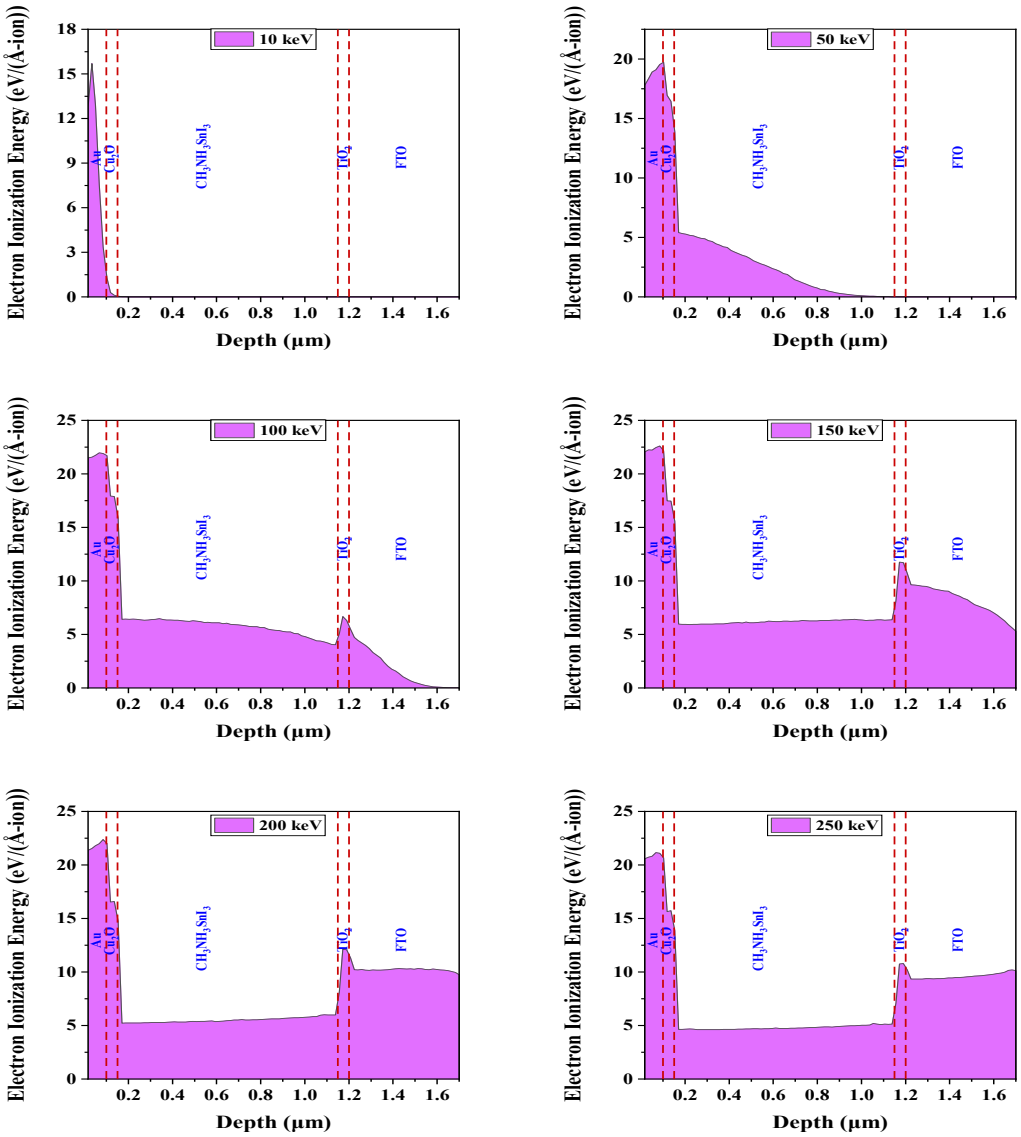


Fig. 9. Electronic stopping power (ionization energy) for 10–250 keV protons as a function of depth.

4.3. Depth-Resolved Electronic Stopping: Electron Ionization Energy

Ionization-energy-loss analysis is crucial because energetic protons induce electronic excitations that expedite chemical degradation, transient defect formation, and lattice destabilization, critical indicators of radiation susceptibility in AM0 environments [44,45]. The fig.9 shows where electronic stopping is the most important in the $Au/Cu_2O/MASnI_3/TiO_2/FTO$ stack. This makes it possible to accurately model the lifetime reduction and electrochemical instability in $MASnI_3$. At 10 keV, ionization loss is limited to Au and Cu_2O, in accordance with high-Z screening. At 50–

100 keV, a lot of electronic excitation happens all over $MASnI_3$, which causes defects to form in Sn-based absorbers. At 150 keV, the peak moves closer to the $MASnI_3/TiO_2$ interface, which means that interfacial recombination is stronger. At 200–250 keV, ionization spreads out a lot and goes deep into TiO_2/FTO. When all the ionization-induced degradation is put together, it happens most strongly between 50 and 150 keV. This shows that this range is very important for designing radiation-tolerant absorbers and interfaces.

4.4. Depth-Resolved Nuclear Stopping: Recoil Energy Loss

Recoil-energy-loss analysis is essential because nuclear-stopping interactions, wherein protons transfer kinetic energy directly to lattice atoms, are the principal mechanisms behind atomic displacements, vacancy–interstitial formation, and long-term structural degradation in photovoltaic materials subjected to space radiation [46]. Mapping recoil-energy deposition across the $Au/Cu_2O/MASnI_3/TiO_2$/FTO stack facilitates authentic SRIM–SCAPS integration for simulating AM0-induced recombination, mobility degradation, and interfacial damage, as depicted in fig.10. At 10 keV, recoil events are limited to Au and Cu_2O, resulting in only superficial knock-on damage. At 50 keV, displacement cascades start to happen at the front of the $MASnI_3$, and at 100 keV, the recoil peak moves deep into the absorber, creating dense, non-recoverable point defects. At 150 keV, the peak nuclear stopping happens close to the $MASnI_3/TiO_2$ interface, which could block pathways for extracting electrons. The recoil energy moves mostly to TiO_2/FTO between 200 and 250 keV. In general, $MASnI_3$ has the most severe displacement damage at 50–150 keV, which is where the Bragg peak is located inside the active layer.

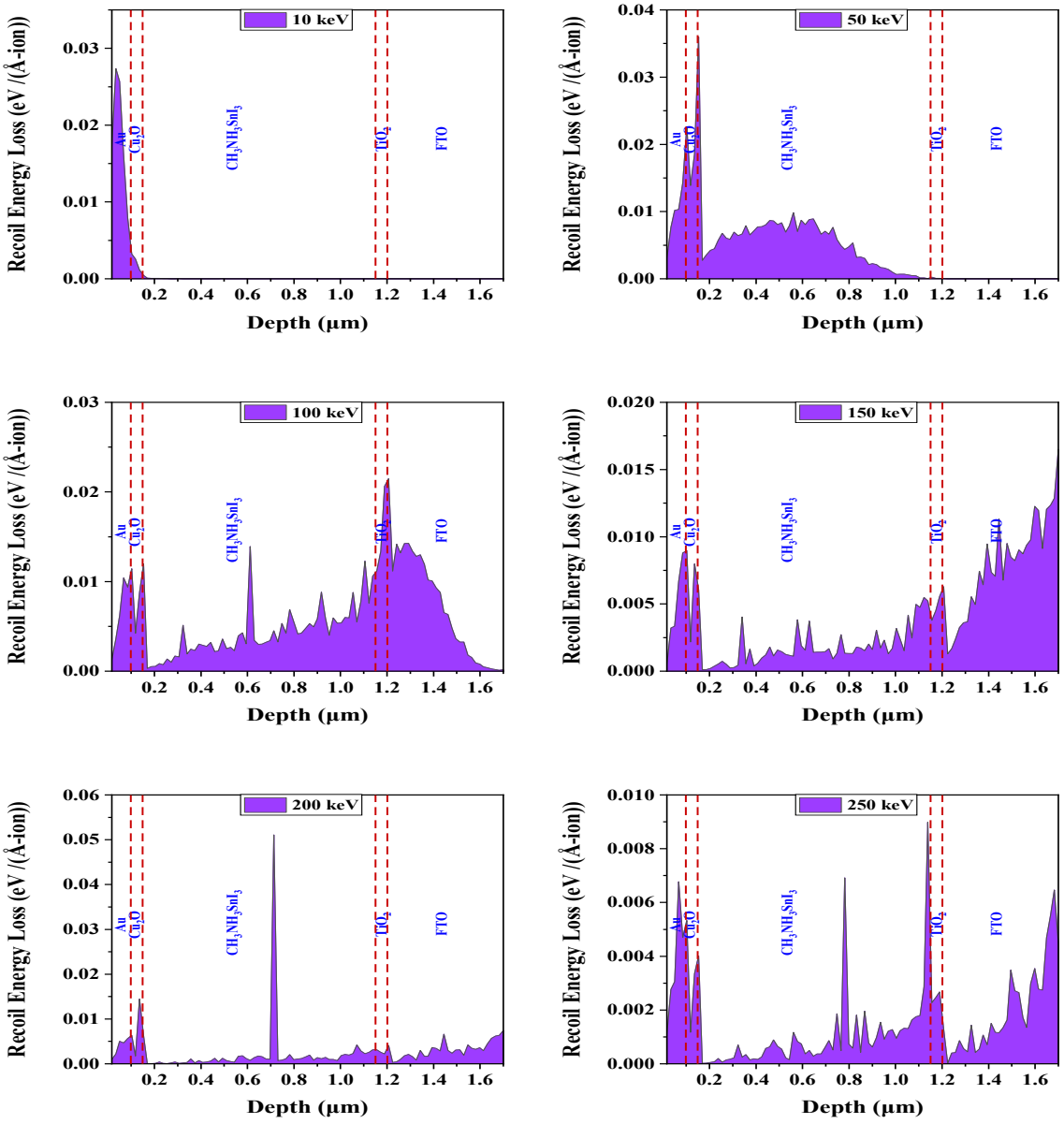


Fig. 10. Recoil energy loss profiles highlighting the nuclear stopping component for each proton energy.

4.5. Spatial Distribution of Total Absorbed Energy

The total-energy-absorption analysis is very important because it tells us how the kinetic energy of protons breaks down into electronic and nuclear stopping across the multilayer stack which gives accurate prediction about how radiation will cause heating, defects, and structural damage in AM0 environments [47,48]. The fig.11 indicates that at 10 keV, almost all proton energy is lost in Au and Cu_2O, which stops the protons from getting into $MASnI_3$ because the high-Z front layers are very strong. At 50 keV, a lot of energy gets to the front $MASnI_3$ area, which is when damage caused by ionization and displacement starts to happen. At 100 keV, the Bragg peak lines up deep within the $MASnI_3$ bulk, causing a lot of energy to be deposited and a lot of defects to build up. The peak moves toward the $MASnI_3/TiO_2$ interface at 150 keV, which means that the electron-extraction junction is more likely to break. TiO_2/FTO absorbs most of the energy between 200 and 250 keV, while $MASnI_3$ gets a weaker, more even dose. These trends show that the 50–150 keV proton-energy band is the most harmful for $MASnI_3$-based space photovoltaics and its charge-selective interfaces thus highlighting the necessity of tailored radiation-hardening strategies for space photovoltaics [49].

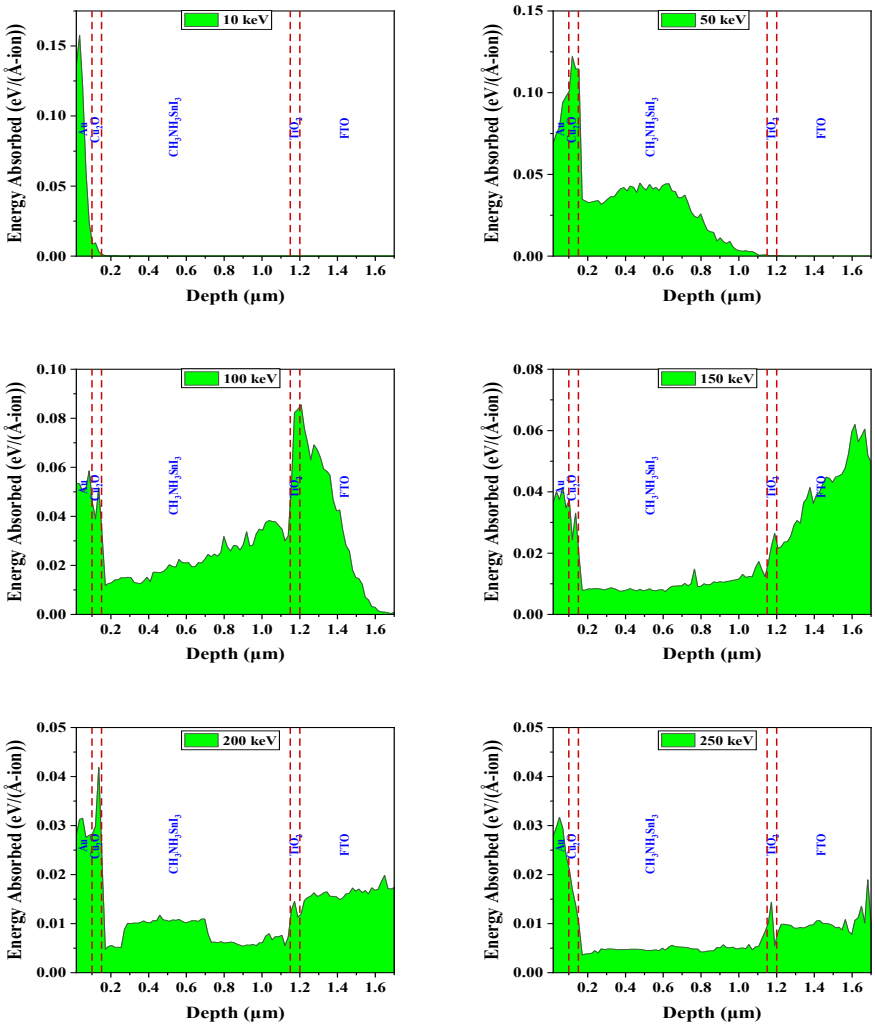


Fig. 11. Total energy absorbed per unit depth for 10–250 keV protons.

4.6. Vacancy Generation by Primary Ions and Recoils

A comparison of the ion-induced and recoil-induced vacancy distributions is desirable, since both primary protons and secondary knock-on cascades generate displacement damage, and its respective contributions need to be separated for an accurate assessment of long-term structural degradation in photovoltaic materials under AM0 proton exposure [50]. The profile data in fig.12 indicate that at 10 keV Au and Cu_2O damage from direct ion effects dominate, with little recoil-induced damage and no ion penetration into $MASnI_3$. At 50 keV, recoil-produced vacancies form in $MASnI_3$ indicating that intermediate energy protons induce multi-step cascades which effectively influence absorber defect creation. At 100 keV, ion- and recoil-induced vacancies both peak in the bulk of $MASnI_3$ at which location the bragg peak is, resulting in greatest defect density and emitter lifetime degradation. At 150 keV, recoil damage moves towards the $MASnI_3/TiO_2$ interface, which goes into TiO_2 and makes it harder for electrons to get out. For 200–250 keV, recoils are mostly found

in TiO_2 and FTO, while $MASnI_3$ has low vacancy formation that is spread out over a wide area. In general, damage to the absorber is mostly caused by recoil in the 50–150 keV range. This range is the most important one for radiation-hardening strategies in perovskite space PVs.

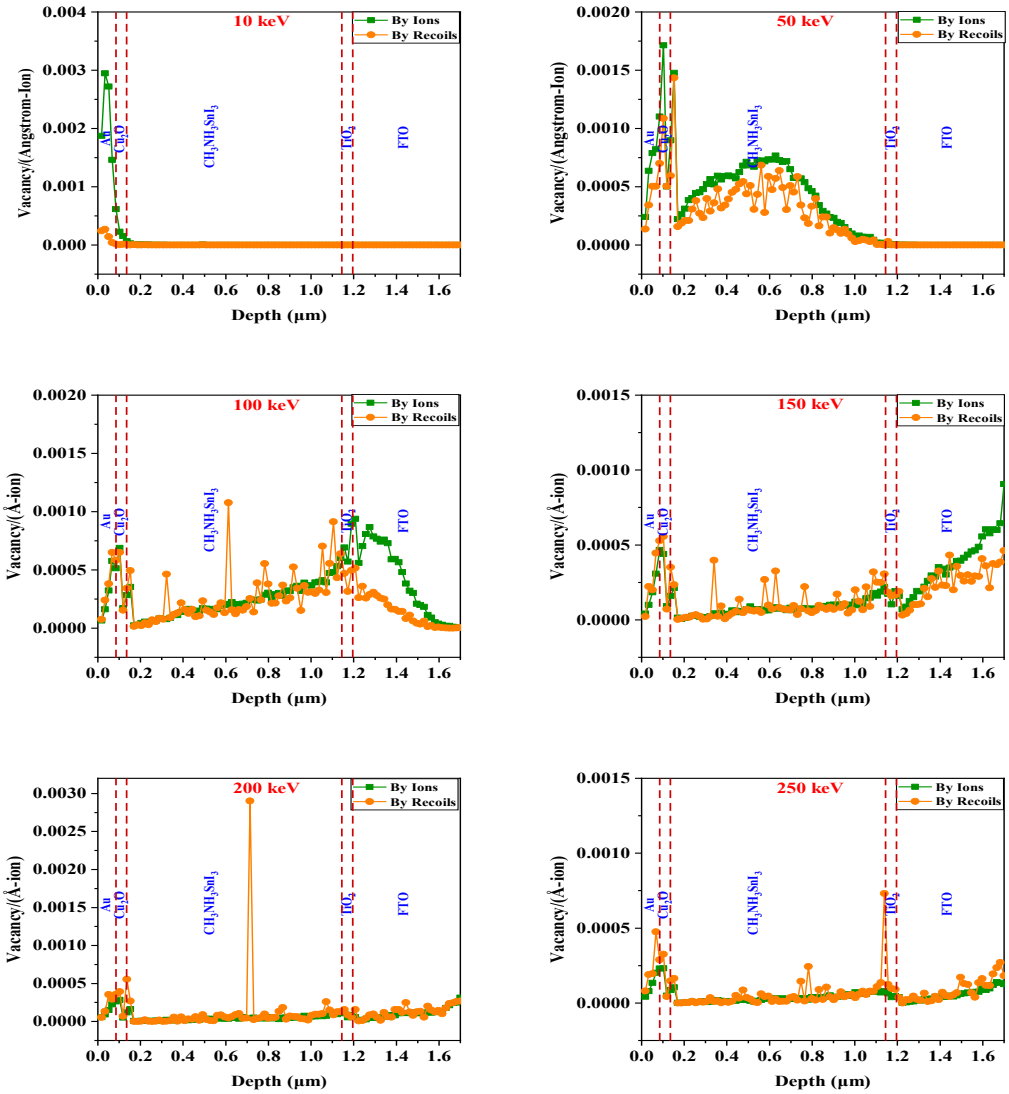


Fig. 12. Depth profiles of vacancies created directly by ions and by recoils at each proton energy.

4.7. Phonon Generation and Lattice Heating Effects

Phonon-generation analysis is essential as lattice vibrations, generated during proton-matter interactions facilitate the dissipation of nuclear and electronic stopping energy which directly affects defect migration process, annealing behaviour and long-term structural instability in perovskite absorber against AM0 radiation [51]. The depth-dependent phonon profile in fig. 13. reveals that at 10 keV, vibrational excitation is limited to Au and Cu_2O; as such protons largely heat high-density front layers without penetrating $MASnI_3$. At 50 keV phonon production extends into the absorber, this suggested that lattice excitation already started. At 100 keV, phonon creation is uniform throughout $MASnI_3$ indicative of more significant bulk excitation which promotes damage formation and decreases carrier lifetimes. The peak at 150 keV moves toward the $MASnI_3/TiO_2$ interface, indicating susceptibility of the junction that extracts electrons. Around 200–250 keV phonons yield optimally in TiO_2, FTO with less uniform excitation in $MASnI_3$. Together, such tendencies pinpoint the 50–150 keV protons as the most destructive energy window needing radiation-hardened designs for space-grade perovskite PVs.

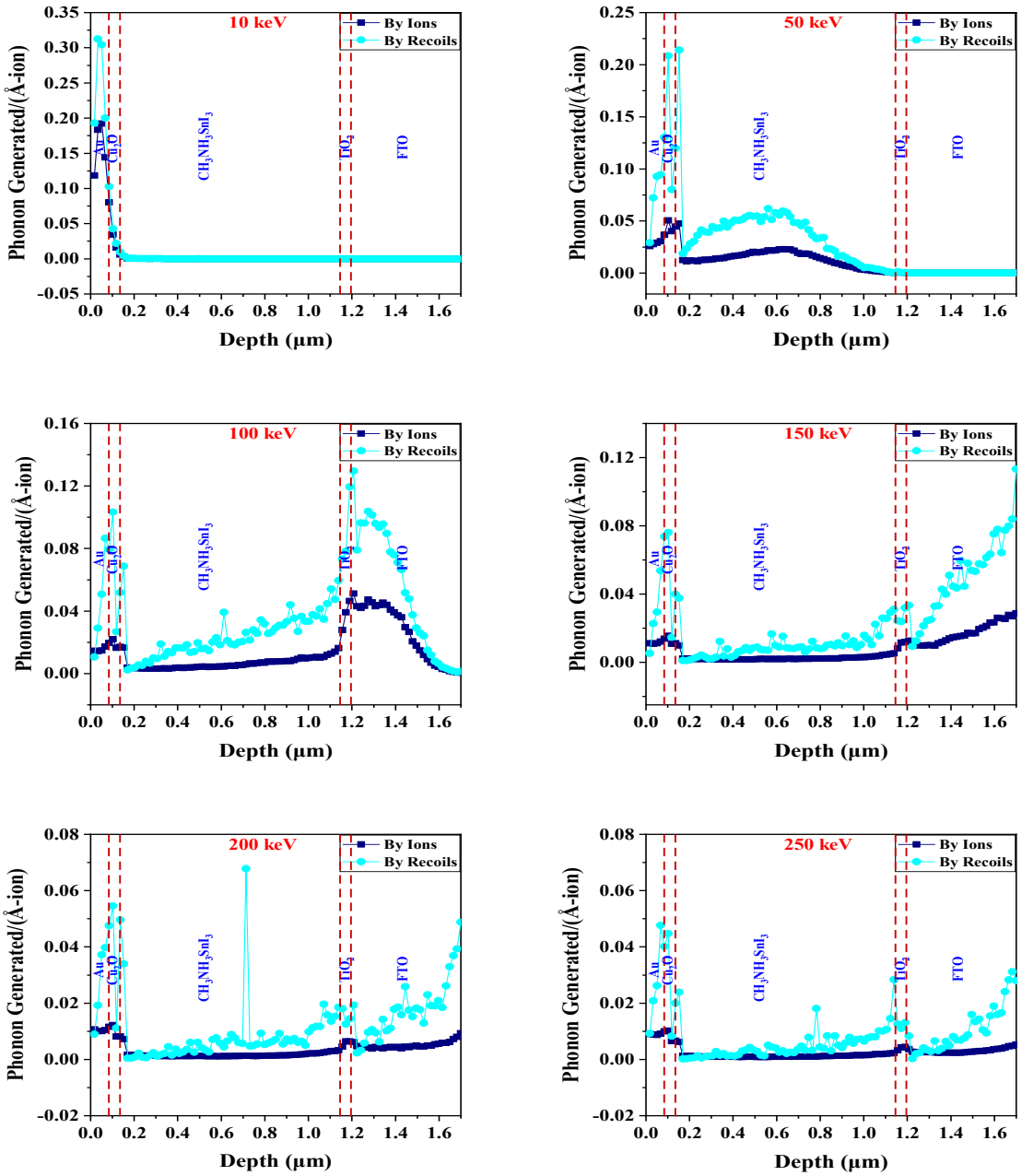


Fig. 13. Depth-resolved phonon generation by ions and recoils for 10–250 keV protons.

5. Quantum Efficiency and J-V Characteristics Under AM1.5 and AM0 Spectra

Characterization of QE and J–V response in respect to AM1.5 as well as AM0 spectrum are imperative since space photovoltaics encounter a significantly different spectral distribution, and precise spectral-response data is crucial for predicting performance and stability under extraterrestrial illumination [52], depicted in fig. 14. The QE of $MASnI_3$ in both conditions is similar, and shows a similar EQE >90% with some blue shift of the absorption edge under AM0 light originating from its richer UV content and high UV absorptivity coefficient as that of $MASnI_3$. The red-edge cutoff around 900-1000 nm originates from the intrinsic $MASnI_3$ bandgap, which serves as a validation that the device efficiently utilizes almost all AM0 photons until its absorption edge. J–V curves exhibit nearly identical V_{OC}, FF, and diode quality under the two spectra, evidencing intrinsic stability for $MASnI_3$ even at high photon flux. Slightly J_{SC} increases under AM0 with superior UV–visible photo-generation feature and maintaining the V_{OC} due to a compatible recombination process. Overall, these results confirm a strong spectral responsivity and diode behavior, re-emphasizing $MASnI_3$'s applicability as light weight, high efficiency AM0 space photovoltaics.

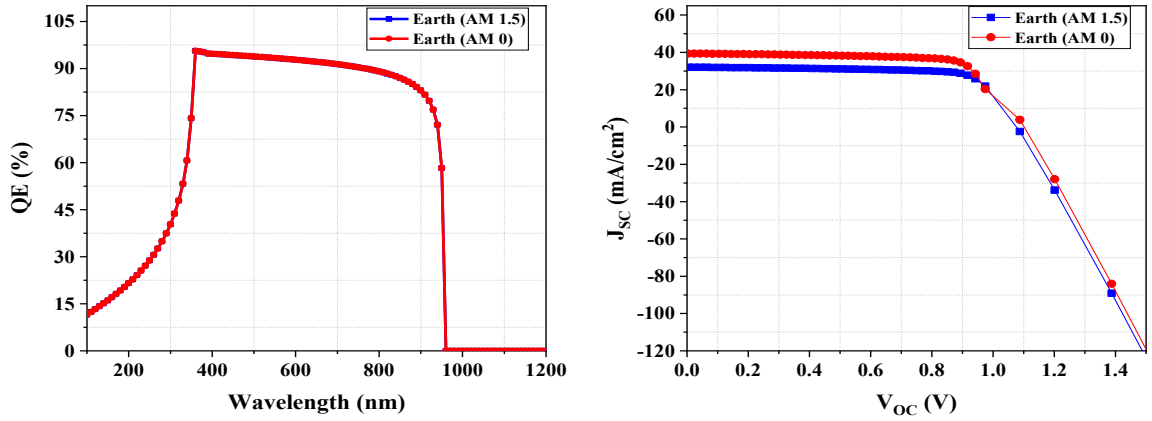


Fig. 14. QE and J-V curves of the optimized device under AM1.5G and AM0 illumination

Table 2. Performance comparison between AM1.5 and AM0 spectral illumination.

Illumination	V_{OC}	J_{SC}	FF	PCE
AM1.5	1.078	32.039	74.36	25.68
AM0	1.086	39.382	72.86	22.85

6. Conclusion

This study develops a unified SCAPS-SRIM optoelectronic exposure co-simulation model to assess $MASnI_3$ perovskite solar cells for space use. Thickness optimization indicates that 0.20–0.30 µm $MASnI_3$, 20–50 nm TiO_2 and 15–30 nm Cu_2O are the optimal ranges for balancing optical absorption, carrier extraction and recombination suppression. J–V and QE measurements under AM1.5 and AM0, $MASnI_3$ devices also showed efficient photogenerated current generation and stable diode characteristics under the spaceable photon flux. SRIM simulations indicate that 50–150 keV protons cause the most significant damage, due to the overlap of BRP with two main features in $MASnI_3$, namely the bulk material and a $MASnI_3/TiO_2$ interface, resulting in high densities of vacancies and strong recoil cascades below and above it as well as a significant phonon excitation. Protons of higher energies (>200 keV) deposit their damage mainly in TiO_2/FTO, thereby keeping the absorber free. The combined SCAPS–SRIM framework we present here thus provides a potent predictive tool for engineering radiation-tolerant perovskite photovoltaics, and the insights gained pinpoint $MASnI_3$ as a highly-encouraging candidate toward realizing lightweight, high-efficiency, and radiation-resilient solar power systems for LEO, MEO, GEO and deep-space missions. This work could be extended by coupling SRIM-derived defect profiles with SCAPS electrical simulations to quantitatively estimate irradiation-induced changes in V_{OC}, J_{SC}, FF and PCE.

All the Declarations and Statements

Author Contributions Statement

Maitry Barua - Conceptualization, Methodology, and Supervision: Proposed research ideas, Constructed the overall framework, and supervised project execution.
Mohammad Mohsin - Drafted the initial manuscript, Data Curation and Software Implementation: Handled data acquisition, dataset preprocessing, and implementing the research model.
Sadman Al Farabe - Formal Analysis, Visualization, and Statistical Analysis, Writing –contributed to the literature survey, and documented the technical background of the study.
Md. Mizanul Hoque – Writing – Review and Editing, and Project Management: Reviewed and edited the manuscript, ensured
clarity and coherence, and helped coordinate project milestones and deadlines.

All authors have read and agreed to the published version of the manuscript.

Conflict of Interest Statement

The authors declare no conflicts of interest.

Funding Declaration

None.

Data Availability Statement

This study analyzed publicly available datasets. The results obtained and datasets can be shared upon email request to: mizan.ruetete08@gmail.com & jitumohsin@gmail.com

Ethical Declarations

This research was conducted following standard ethical and academic guidelines. The study mainly involved simulation-based analysis and did not include any harmful experiments on humans or animals.

Acknowledgments

The authors would like to express their sincere gratitude to Bangladesh Satellite Company Limited (BSCL) for providing the opportunity to conduct this research under its Internship Program (Bengali Name: "বাংলাদেশ তারুণ্যের উৎসব ২০২৫"). The continuous guidance, technical support, and research-friendly environment offered by BSCL greatly contributed to the successful completion of this work.

The authors also acknowledge the valuable cooperation and encouragement received from the research team members, supervisors, and concerned officials throughout the study. Their support and constructive suggestions played an important role in the preparation and publication of this journal article.

Declaration of Generative AI in Scholarly Writing

During the preparation of this manuscript, limited AI-assisted tools were used only for language refinement, grammar checking, and formatting improvement. All research design, simulations, technical analysis, result interpretation, and conclusions were independently conducted and verified by the author. The author takes full responsibility for the originality and content of this manuscript.

Abbreviations

The following abbreviations are used in this manuscript:

LEO - Low Earth Orbit
MEO - Medium Earth Orbit
GEO - Geostationary Earth Orbit
PCE - Power Conversion Efficiency
J_{SC} – Short Circuit Current Density
V_{OC} – Oper Circuit Voltage
FF – Fill Factor
DFT – Density Functional Theory
ETL – Electron Transport Layer
HTL – Hole Transport Layer

References

[1] Verduci R, Romano V, Brunetti G, Yaghoobi Nia N, Di Carlo A, D'Angelo G, et al. Solar Energy in Space Applications: Review and Technology Perspectives. Adv Energy Mater 2022;12. https://doi.org/10.1002/aenm.202200125.
[2] Noman M, Khan Z, Jan ST. A comprehensive review on the advancements and challenges in perovskite solar cell technology. RSC Adv 2024;14:5085–131. https://doi.org/10.1039/d3ra07518d.
[3] Pessoa RS, Fraga MA. Recent advances in solar cells for aerospace applications: Materials and technologies. J Aerosp Technol Manag 2023;15. https://doi.org/10.1590/jatm.v15.1296.
[4] Romano V, Agresti A, Verduci R, D'Angelo G. Advances in Perovskites for Photovoltaic Applications in Space. ACS Energy Lett 2022;7:2490–514. https://doi.org/10.1021/acsenergylett.2c01099.
[5] Bush ME, Sims JD, Erickson SS, VanSant KT, Ghosh S, Luther JM, et al. Space environment considerations for perovskite solar cell operations: A review. Acta Astronaut 2025;235:235–50. https://doi.org/10.1016/j.actaastro.2025.05.025.
[6] Reb LK, Böhmer M, Predeschly B, Grott S, Weindl CL, Ivandekic GI, et al. Perovskite and Organic Solar Cells on a Rocket Flight. Joule 2020;4:1880–92. https://doi.org/10.1016/j.joule.2020.07.004.
[7] Vanitha L, Thandaiah Prabu R, Subha TD, Kumar A. Computational analysis of perovskite solar cells for space applications. J Comput Electron 2025;24:91. https://doi.org/10.1007/s10825-025-02335-0.
[8] Barua M, Hayat Khan MY, Hasan MZ, Ahamed JU. Halogen engineering in lead-free Mg3PX3 perovskites: A first-principles investigation for UV to IR optoelectronic and photovoltaic applications. Comput Condens Matter 2026;46.

https://doi.org/10.1016/j.cocom.2026.e01220.
[9] Zhao P, Su J, Guo Y, Wang L, Lin Z, Zhang J, et al. A new all-inorganic vacancy-ordered double perovskite Cs2CrI6 for high-performance photovoltaic cells and alpha-particle detection in space environment. Mater Today Phys 2021;20. https://doi.org/10.1016/j.mtphys.2021.100446.
[10] Zhang W, Sun C, Liu K, Shen W, Wu Y, Yao L, et al. Technical challenges of space solar power stations: Ultra-large-scale space solar array systems and space environmental effects. Sp Sol Power Wirel Transm 2024;1:69–87. https://doi.org/10.1016/j.sspwt.2024.09.003.
[11] Huan Z, Zheng Y, Wang K, Shen Z, Ni W, Zu J, et al. Advancements in radiation resistance and reinforcement strategies of perovskite solar cells in space applications. J Mater Chem A 2024;12:1910–22. https://doi.org/10.1039/d3ta06388g.
[12] Kareem M, Thaban B, Rajiv A, Sahu BN, Sundharam S, Tomar P. Multiscale simulation of eco-friendly perovskites under space radiation. Nanoscale 2026. https://doi.org/10.1039/D5NR03859F.
[13] Magdalin AE, Nixon PD, Jayaseelan E, Sivakumar M, Devi SKN, Subathra MSP, et al. Development of lead-free perovskite solar cells: Opportunities, challenges, and future technologies. Results Eng 2023;20. https://doi.org/10.1016/j.rineng.2023.101438.
[14] Islam B, Khan TM, Rahaman MM, Ahmed SR Al. Computational optimization of MASnI3 perovskite solar cells using SCAPS-1D simulations and machine learning techniques. RSC Adv 2026;16:1172–92. https://doi.org/10.1039/D5RA07200J.
[15] Sajid S, Alzahmi S, Salem I Ben, Park J, Obaidat IM. Lead-Free Perovskite Homojunction-Based HTM-Free Perovskite Solar Cells: Theoretical and Experimental Viewpoints. Nanomaterials 2023;13. https://doi.org/10.3390/nano13060983.
[16] Singh AK, Srivastava S, Mahapatra A, Baral JK, Pradhan B. Performance optimization of lead free-MASnI3 based solar cell with 27% efficiency by numerical simulation. Opt Mater (Amst) 2021;117. https://doi.org/10.1016/j.optmat.2021.111193.
[17] Ivriq SB, Mohammadi MH, Davidsen RS. Enhancing photovoltaic efficiency Perovskite solar cells with triple core-shell plasmonic nanoparticles 2025:1–22.
[18] Chen H, Li C, Zhou W, Wen J, Ma M, Chen Y, et al. Designing and optimizing the lead-free double perovskite Cs2AgBiI6/Cs2AgBiBr6 bilayer perovskite solar cell. Sol Energy 2024;284. https://doi.org/10.1016/j.solener.2024.113087.
[19] Mohammed MKA, Al-Azraq BT, Al-Mousoi AK, Salih EY, Rajiv A, Sahu BN, et al. Multiphysics insights into CsPbI3 perovskite photovoltaics under proton irradiation. Renew Energy 2026;256. https://doi.org/10.1016/j.renene.2025.124571.
[20] Kirmani AR, Byers TA, Ni Z, VanSant K, Saini DK, Scheidt R, et al. Unraveling radiation damage and healing mechanisms in halide perovskites using energy-tuned dual irradiation dosing. Nat Commun 2024;15. https://doi.org/10.1038/s41467-024-44876-1.
[21] Samantaray MR, Wong TL, Mondal A kumar, Pescetelli S, Lee DJ, Muñoz-Castro A, et al. Lead-Free MaSnI3/Sb2S3 Heterojunction Solar Cell with Power Conversion Efficiency Approaching 30%: A SCAPS-1D Simulation Study. Sol RRL 2025. https://doi.org/10.1002/solr.202500642.
[22] Hossain MK, Rubel MHK, Toki GFI, Alam I, Rahman MF, Bencherif H. Effect of Various Electron and Hole Transport Layers on the Performance of CsPbI3-Based Perovskite Solar Cells: A Numerical Investigation in DFT, SCAPS-1D, and wxAMPS Frameworks. ACS Omega 2022;7:43210–30. https://doi.org/10.1021/acsomega.2c05912.
[23] Gao Y, Jiang H, Zhang W, Ying Y, Chen L, Han L, et al. Design and Numerical Optimization of Dual Interface Layers for MASnI3Perovskite Solar Cells Based on SCAPS-1D Simulation. Langmuir 2025;41:26030–43. https://doi.org/10.1021/acs.langmuir.5c02645.
[24] Oryema B, Madiba IG, Mtshali CB. Atomistic Simulation of Primary Radiation Damage Profiles in Fluorine-Doped Tin Oxide Thin Film Target Using SRIM Code. Nano-Horizons J Nanosci Nanotechnologies 2024;3. https://doi.org/10.25159/3005-2602/15610.
[25] Raj M, Makhija A, Kushwaha A, Goel N. Integrated First-Principles, SCAPS-1D, and ML Framework for Engineering $CsAgBiBr_6$ based Perovskite Solar Cell for IoT-Integrated Applications. Mater Sci Eng B 2026;324:119014. https://doi.org/https://doi.org/10.1016/j.mseb.2025.119014.
[26] MallaHasan H, Onay Ö. Investigation of the effect of different factors on the performance of several perovskite solar cells: a simulation study by SCAPS. Eur J Eng Sci Technol 2022;5:20–38. https://doi.org/10.33422/ejest.v5i1.927.
[27] Shim H, Seo S, Chandler C, Sharpe MK, McAleese CD, Lim J, et al. Enhancing radiation resilience of wide-band-gap perovskite solar cells for space applications via A-site cation stabilization with PDAI2. Joule 2025;9. https://doi.org/10.1016/j.joule.2025.102043.
[28] Angela E, Nodari D, Furlan F, Panidi J, McLachlan MA, Gasparini N. Blending Self-Assembled Monolayers for Enhanced Band Alignment and Improved Morphology in p-i-n Perovskite Photodetectors. ACS Appl Mater Interfaces 2024;16:33838–45. https://doi.org/10.1021/acsami.4c06447.
[29] Mortadi A, El Hafidi EM, Sadiqi A, Nasrellah H, Laasri S, Chahid E ghaouti, et al. Thickness-dependent performance optimization of lead-free FASnI3 perovskite solar cells: Interplay between optical absorption and charge recombination. Hybrid Adv 2025;11. https://doi.org/10.1016/j.hybadv.2025.100528.
[30] Gwandu BU, Nawawi YH, Faruk S, Zauro AS. Numerical investigation on the impact of Hole Transporting Layer (HTL) using SCAPS-1D on tin-based perovskite solar cells. Equity J Sci Technol 2023;10:10–6.
[31] Edam MJ, Mahdi AS, AbdulAlmohsin SM, Khadier HM. Perovskites Solar Cells Study Optimization Thickness, Temperature and Work Function. J Nanostructures 2025;15:1208–19. https://doi.org/10.22052/JNS.2025.03.038.
[32] Tuo S, Kamenan KA, Coulibaly AB. Simulation of a Perovskite Solar Cell with High Efficiency Using Various Hole Transport Layers. Cryst Struct Theory Appl 2025;13:1–13. https://doi.org/10.4236/csta.2025.131001.
[33] Mohsin M, Anan MI, Datta PG, Das K, Al Islam MW, Niloy AB, et al. Energy harvesting from Cs2CuBiX6 solar cells: A comparison of efficiency and improvement. J Phys Chem Solids 2025;200:112611. https://doi.org/https://doi.org/10.1016/j.jpcs.2025.112611.
[34] Rayhan A, Khan MA, Islam MR. Enhancing CsSn0.5Ge0.5I3 Perovskite Solar Cell Performance via Cu2O Hole Transport Layer Integration. Int J Photoenergy 2024;2024. https://doi.org/10.1155/2024/8859153.
[35] Siddique A, Nurul Islam M, Karmaker H, Asif Iqbal AKM, Al Mazed Khan A, Aminul Islam M, et al. Numerical modelling and

performance investigation of inorganic Copper-Tin-Sulfide (CTS) based perovskite solar cell with SCAPS-1D. Results Opt 2024;16. https://doi.org/10.1016/j.rio.2024.100713.
[36] Rshash HA, Abdul Almohsin SM. Optimization of Thickness, Energy Band Gap, and Temperature for High Efficiency of Lead Halide Perovskite Solar Cell. Int J Thin Film Sci Technol 2024;13:225–33. https://doi.org/10.18576/ijtfst/130307.
[37] Islam S, Hossain MK, Uddin MS, Prabhu P, Ballal S, Vinay KP, et al. A numerical investigation to design and performance optimization of lead-free Cs2TiCl6based perovskite solar cells with different charge transport layers. Sci Rep 2025;15. https://doi.org/10.1038/s41598-025-06820-1.
[38] Atem M Al, Dridi Rezgui B, Touhami I, Bouaïcha M. Numerical simulation and optimization of high-performance lead-based $FAMACsPb(IBr)_3$ perovskite solar cells using SCAPS 1D. Results Eng 2026;29:108555. https://doi.org/10.1016/j.rineng.2025.108555.
[39] Treglia A, Ambrosio F, Martani S, Folpini G, Barker AJ, Albaqami MD, et al. Effect of electronic doping and traps on carrier dynamics in tin halide perovskites. Mater Horizons 2022;9:1763–73. https://doi.org/10.1039/d2mh00008c.
[40] Costa C, Manceau M, Duzellier S, Nuns T, Cariou R. Perovskite solar cells under protons irradiation: From in-situ IV-monitoring to root cause degradation elucidation. Sol Energy Mater Sol Cells 2023;257. https://doi.org/10.1016/j.solmat.2023.112388.
[41] Nguyen D-T, Walter D, Weber K, White T, Duong T. A Research on Perovskite Solar Cells' Tolerance under Proton Radiations. 2023.
[42] Erickson S, Lum C, Stephens K, Parashar M, Saini DK, Rout B, et al. Elucidating early proton irradiation effects in metal halide perovskites via photoluminescence spectroscopy. IScience 2025;28. https://doi.org/10.1016/j.isci.2024.111586.
[43] Rasmetyeva A V., Zyryanov SS, Novoselov IE, Kukharenko AI, Makarov E V., Cholakh SO, et al. Proton Irradiation on Halide Perovskites: Numerical Calculations. Nanomaterials 2024;14. https://doi.org/10.3390/nano14010001.
[44] Nguyen DT, Walter D, Weber KJ, Duong T, White TP. Simulating Proton Radiation Tolerance of Perovskite Solar Cells for Space Applications. Adv Energy Sustain Res 2023;4. https://doi.org/10.1002/aesr.202300085.
[45] Song S, Cho HW, Kim H, Kim M, Kim G-H. Perovskite solar cells for low earth orbit space applications. Energy Mater 2026;6:600019. https://doi.org/10.20517/energymater.2025.162.
[46] Martinez Duque RB, Kirmani AR, Sellers IR, Borunda MF. Threshold Displacement Energies in Lead Halide Perovskites from Ab Initio Molecular Dynamics Simulations. PRX Energy 2025;4. https://doi.org/10.1103/PRXEnergy.4.013006.
[47] Hughes D, Meroni SMP, Barbé J, Raptis D, Lee HKH, Heasman KC, et al. Proton Radiation Hardness of Perovskite Solar Cells Utilizing a Mesoporous Carbon Electrode. Energy Technol 2021;9. https://doi.org/10.1002/ente.202100928.
[48] Herrera Martínez WO, Correa Guerrero NB, Gómez Andrade VA, Alurralde M, Perez MD. Evaluation of the resistance of halide perovskite solar cells to high energy proton irradiation for space applications. Sol Energy Mater Sol Cells 2022;238. https://doi.org/10.1016/j.solmat.2022.111644.
[49] Zhang L, Li S, Wang Y, Li H, Chen R, Zhu X, et al. Comparative study on radiation resistance of tin–lead and pure lead perovskite solar cells. Mater Adv 2025;6:8490–6. https://doi.org/10.1039/D5MA00737B.
[50] Nordlund K, Zinkle SJ, Sand AE, Granberg F, Averback RS, Stoller R, et al. Improving atomic displacement and replacement calculations with physically realistic damage models. Nat Commun 2018;9. https://doi.org/10.1038/s41467-018-03415-5.
[51] Kishor A, Raj A, Raj M, Goel N. Proton radiation impact on bilayer perovskite solar cells for space Application: A comprehensive SCAPS, DFT and ML study. J Phys Chem Solids 2026;209:113302. https://doi.org/https://doi.org/10.1016/j.jpcs.2025.113302.
[52] McMillon-Brown L, Luther JM, Peshek TJ. What Would It Take to Manufacture Perovskite Solar Cells in Space? ACS Energy Lett 2022;7:1040–2. https://doi.org/10.1021/acsenergylett.2c00276.

Authors' Profiles



Maitry Barua, received the B.Sc. degree in Electrical and Electronic Engineering (EEE) in 2024. She is presently pursuing the M.Sc. degree in Electrical and Electronic Engineering in the Department of Electrical and Electronic Engineering, University of Chittagong, Chattogram, Bangladesh. Her research interests include first-principles DFT calculations, electronic structure analysis, and solar and renewable energy related materials.



Mohammad Mohsin, received B. Sc. in year 2023. He is pursuing M. Sc. in Electrical and Electronic Engineering from University of Chittagong. His interest is in solar cell's space application.



Sadman Al Farabe, (Masters Student,CUET) received Bachelor of Engineering in Electrical Electronics Engineering from Daffodil International University in 2016 and now pursuing a Master's degree in Telecommunications Engineering from Chittagong University of Engineering Technology (CUET) and now working as a Radio Frequency Engineer at a Satellite Ground Station from 2017–2024. My research topics mainly include 6G Telecommunications, Antenna Design, RF Engineering, Terahertz Communication.



Md. Mizanul Hoque, (PhD Student, BUP) received the B.Sc. degree in Electronics and Telecommunication Engineering from Rajshahi University of Engineering and Technology (RUET), Bangladesh, in 2014, and the M.Sc. degree in Information and Communication Technology from Bangladesh University of Professionals (BUP), in 2019. Since 2014. He worked at Robi Axiata Ltd. as an Optical Transmission Network professional. Then, in 2019, he began working at the Ministry of Defense, Bangladesh as a System Analyst. He now works for Bangladesh Satellite Company Limited (BSCL) as a Manager, Network Engineer- Broadcast. He is presently a Ph.D. student at Bangladesh University of Professionals (BUP) studying 6G wireless communication. He has several research articles that have been published in journals and conferences throughout the world. His current areas of interest in research include Free Space Optical (FSO), Interplanetary Communication, and Next-Generation Wireless Communications.

How to cite this paper

Maitry Barua, Mohammad Mohsin, Sadman Al Farabe, Mizanul Hoque, "Radiation-Tolerant $MASnI_3$ Perovskite Solar Cells for Space Communication: Sequential SCAPS Optimization and SRIM-Based Proton Damage Analysis", International Journal of Wireless and Microwave Technologies(IJWMT), Vol.16, No.3, pp. 305-322, 2026. DOI:10.5815/ijwmt.2026.03.20